AGU PUBLICATIONS

Geophysical Research Letters

RESEARCH LETTER
10.1002/2017GL074215

Key Points:
- NH_3 gas-to-aerosol partitioning induces regional differences between NH_3 emission factors derived from in situ and satellite observations
- Greatest partitioning is over large savanna and tropical forest fires, where NO emissions exceed those of NH_3, promoting NH_4NO_3 production
- Fires can contribute over 20% of the NH_4NO_3 burden and associated radiative effect despite accounting for less than 6% of NH_3 emissions

Supporting Information:
- Supporting Information S1

Correspondence to:
F. Paulot,
Fabien.Paulot@noaa.gov

Citation:
Paulot, F., D. Paynter, P. Ginoux, V. Naik, S. Whitburn, M. Van Damme, L. Clarisse, P.-F. Coheur, and L. W. Horowitz (2017), Gas-aerosol partitioning of ammonia in biomass burning plumes: Implications for the interpretation of spaceborne observations of ammonia and the radiative forcing of ammonium nitrate, *Geophys. Res. Lett.*, *44*, 8084–8093, doi:10.1002/2017GL074215.

Received 22 MAY 2017
Accepted 27 JUL 2017
Accepted article online 2 AUG 2017
Published online 14 AUG 2017

Gas-aerosol partitioning of ammonia in biomass burning plumes: Implications for the interpretation of spaceborne observations of ammonia and the radiative forcing of ammonium nitrate

F. Paulot[1,2], D. Paynter[2], P. Ginoux[2], V. Naik[2], S. Whitburn[3], M. Van Damme[3], L. Clarisse[3], P.-F. Coheur[3], and L. W. Horowitz[2]

[1]Program in Atmospheric and Oceanic Sciences, Princeton University, Princeton, New Jersey, USA, [2]Geophysical Fluid Dynamics Laboratory, National Oceanic and Atmospheric Administration, Princeton, New Jersey, USA, [3]Université Libre de Bruxelles, Atmospheric Spectroscopy, Service de Chimie Quantique et Photophysique, Brussels, Belgium

Abstract Satellite-derived enhancement ratios of NH_3 relative to CO column burden ($ER_{NH_3/CO}$) in fires over Alaska, the Amazon, and South Equatorial Africa are 35, 45, and 70% lower than the corresponding ratio of their emissions factors ($EF_{NH_3/CO}$) from biomass burning derived from in situ observations. Simulations performed using the Geophysical Fluid Dynamics Laboratory AM3 global chemistry-climate model show that these regional differences may not entirely stem from an overestimate of NH_3 emissions but rather from changes in the gas-aerosol partitioning of NH_3 to NH_4^+. Differences between $ER_{NH_3/CO}$ and $EF_{NH_3/CO}$ are largest in regions where EF_{NO_x/NH_3} is high, consistent with the production of NH_4NO_3. Biomass burning is estimated to contribute 11–23% of the global burden and direct radiative effect (DRE) of NH_4NO_3 (−15 to −28 mW m^{-2}), despite accounting for less than 6% of the global source of NH_3. Production of NH_4NO_3 is largely concentrated over the Amazon and South Equatorial Africa, where its DRE can reach −1.9 W m^{-2} during the biomass burning season.

1. Introduction

Biomass burning is the largest natural source of NH_3 on land [*Bouwman et al.*, 1997; *Paulot et al.*, 2014]. The emissions of NH_3 from fires and subsequent NH_3 deposition play an important role in the redistribution of nitrogen, a limiting nutrient in many ecosystems, from savanna to tropical forests [*Chen et al.*, 2010]. However, the magnitude of the biomass burning source of NH_3 remains highly uncertain as is illustrated by the large differences between the Global Fire Assimilation System (6.33 TgN a^{-1}) [*Kaiser et al.*, 2012] and the Global Fire Emissions Database (GFED v4.1s; 3.35 TgN a^{-1}) [*van der Werf et al.*, 2010; *Randerson et al.*, 2012] over the 2003–2008 period. This large range primarily reflects the uncertainty in emission factors for NH_3 (EF_{NH_3}), the mass of NH_3 emitted per kilogram of dry matter burnt. EF_{NH_3} is generally derived from in situ observations in fresh plumes [*Akagi et al.*, 2011]. Ground-based [*Paton-Walsh et al.*, 2005; *Lutsch et al.*, 2016] and, more recently, spaceborne instruments, such as the Infrared Atmospheric Sounding Interferometer (IASI) [*Coheur et al.*, 2009; *R'Honi et al.*, 2013; *Whitburn et al.*, 2015, 2016a] and the Tropospheric Emission Spectrometer (TES) [*Luo et al.*, 2015; *Alvarado et al.*, 2011], have also been used to quantify the enhancement of NH_3 over fires. Two approaches have been used to estimate NH_3 emissions from remote sensing. In the first approach, EF_{NH_3} is estimated using the ratio of the enhancement of NH_3 relative to the enhancement of another species (typically CO, $ER_{NH_3/CO}$), for which fire emissions are well characterized [*Coheur et al.*, 2009; *R'Honi et al.*, 2013; *Whitburn et al.*, 2016a; *Alvarado et al.*, 2011; *Luo et al.*, 2015]. This approach does not take into account the effect of aging, including chemical loss, physical deposition, and gas-aerosol partitioning, which can alter the relationship between enhancement ratio and emission ratio [*Yokelson et al.*, 2013]. In the case of NH_3, $ER_{NH_3/CO}$ is expected to underestimate EF_{NH_3}, as the lifetime of NH_3 is much shorter than that of CO [*Whitburn et al.*, 2016a]. In the second approach, the regional emissions of NH_3 are estimated from a box model constrained by daily changes in the regional NH_3 burden [*Whitburn et al.*, 2015, 2016a], assuming a first-order loss of NH_3 (i.e., $d[NH_3]/dt = -k[NH_3]$). This approach is susceptible to other sources of NH_3 (e.g., agriculture) and sensitive

to the choice of lifetime for NH_3 ($\tau_{NH_3} = 1/k$) in the plume [*Whitburn et al.*, 2015]. τ_{NH_3} is generally assumed to range from 12 to 36 h following estimates derived from global models [*Whitburn et al.*, 2015], which is consistent with recent observations from Canadian fires ($\tau_{NH_3} = 48$h) [*Lutsch et al.*, 2016]. However, the lifetime of NH_3 may be much shorter in some biomass burning plumes, as a result of its rapid reactions with SO_4^{2-} and HNO_3, a product of NO oxidation, to form $(NH_4)_xH_{2-x}SO_4$ ($x \leq 2$) and NH_4NO_3 aerosol. For instance, *Yokelson et al.* [2009] estimated that 30% of the emitted NH_3 was converted to NH_4^+ within 1.4 h of the emission and similar conversion rates can be inferred from recent observations for agricultural fires [*Liu et al.*, 2016]. Note that these gas-to-aerosol partitioning reactions are limited by the availability of reactants and may not be adequately represented by first-order loss processes in aged plumes.

In situ observations have shown that NH_4NO_3 is produced rapidly after emission [*Hobbs et al.*, 2003; *Yokelson et al.*, 2009; *Alvarado et al.*, 2010; *Hecobian et al.*, 2011; *Akagi et al.*, 2012; *Liu et al.*, 2016; *Collier et al.*, 2016; *Cai et al.*, 2016; *Benedict et al.*, 2017]. NH_4NO_3 formation is promoted by high concentrations of $TNH_3 \equiv NH_3 + NH_4^+$ and $TNO_3 \equiv HNO_3 + NO_3^-$ and low temperature (associated with injection of smoke into the free troposphere) consistent with the thermodynamic equilibrium between NH_3/HNO_3 gases and NH_4NO_3 aerosols [*Stelson and Seinfeld*, 1982]. Such conditions are often not met for anthropogenic sources, as NO_x emissions (mostly from fossil fuel) and NH_3 emissions (mostly from agriculture) can be spatially segregated [*Pinder et al.*, 2007; *Paulot and Jacob*, 2014] and emitted at the surface. As a result, NH_4NO_3 concentration is often low in summer in the midlatitudes [*Schaap et al.*, 2004; *Heald et al.*, 2012; *Paulot et al.*, 2016]. This suggests that biomass burning, a minor source of NH_3 (~10%) [*Paulot et al.*, 2014], may have a disproportionate importance in the global budget of NH_4NO_3. Although this contribution has not been quantified to date, global model simulations show that the direct radiative forcing (DRF) of NH_4NO_3 ($DRF_{NH_4NO_3}$) is stronger than -1 W m^{-2} over tropical biomass burning sources [*Hauglustaine et al.*, 2014], a value which is comparable to $DRF_{NH_4NO_3}$ over large agricultural sources of NH_3 in Europe and the U.S.

Here we use retrievals of CO and NH_3 column burdens for 2009–2013 from IASI to calculate the enhancement of NH_3 relative to CO in three different world regions. We then use the Geophysical Fluid Dynamics Laboratory (GFDL) global chemistry-climate model AM3 to estimate the influence of aging on $ER_{NH_3/CO}$. Finally, we discuss the influence of biomass burning on the budget and direct radiative effect of NH_4NO_3.

2. Method

We use morning observations (overpass time 9:30 A.M. LT over the equator) of CO [*Hurtmans et al.*, 2012] and NH_3 [*Whitburn et al.*, 2016b] total columns from IASI on board the Metop A satellite. Observations (footprints of 12 km at nadir) are regridded to 0.5° × 0.5° by taking the arithmetic mean of all measurements within a cell. Following *Whitburn et al.* [2016a], we only consider NH_3 columns with relative errors lower than 100% or absolute errors lower than 7.5×10^{15} mol cm^{-2} and exclude scenes with cloud contamination greater than 25%. Both CO and NH_3 retrievals have been used in previous studies to characterize the biomass burning sources of NH_3 at high latitudes [*R'Honi et al.*, 2013] and in the tropics [*Whitburn et al.*, 2015, 2016a].

We use the GFDL-AM3 model [*Donner et al.*, 2011; *Naik et al.*, 2013], the atmospheric chemistry-climate component of the GFDL-CM3 model [*Donner et al.*, 2011; *Griffies et al.*, 2011; *John et al.*, 2012], to simulate the fate of NH_3 emitted from biomass burning. We include recent updates to AM3 chemistry and wet deposition described [*Paulot et al.*, 2016, 2017]. The formation of NH_4NO_3 is assumed to be controlled by the thermodynamic equilibrium between $TNH_3 \equiv NH_3 + NH_4^+$, $TSO_4 \equiv H_2SO_4 + HSO_4^- + SO_4^{2-}$, and $TNO_3 \equiv HNO_3 + NO_3^-$, which is solved using ISORROPIA [*Fountoukis and Nenes*, 2007] at each model time step (30 min). *Paulot et al.* [2016] showed that this version of AM3 captures the seasonal and spatial distributions of surface $[NO_3^-]$ in Europe and the U.S. well ($R > 0.6$), which indicates that AM3 can provide insights on the sensitivity of $[NH_3]$ to the absolute and relative magnitudes of NO_x (via HNO_3) and NH_3 emissions. NH_4NO_3 optical properties are obtained from Mie calculations using hygroscopic growth from *Tang* [1996] and refractive indices from *Gosse et al.* [1997]. Hygroscopic growth is capped at 97% for all aerosols. We also account for the formation of coarse-mode NO_3^- through the uptake of HNO_3 on dust, but its radiative forcing is not considered. *Hauglustaine et al.* [2014] estimated that coarse-mode NO_3^- accounts for 10% of the overall NO_3^- radiative forcing.

Daily dry matter emissions are obtained from the Global Fire Emissions Database (GFEDv4.1s) [*Giglio et al.*, 2010; *Randerson et al.*, 2012] and speciated using recommended emission factors (EFs) [*Andreae and Merlet*, 2001; *Akagi et al.*, 2011]. We follow *Sofiev et al.* [2012, 2013] and *Mu et al.* [2011] to distribute emissions

vertically and hourly, respectively. To account for rapid chemistry in the plume, oxidized nitrogen is emitted as peroxyacetyl nitrate (40%), NO (40%), and nitric acid (20%) rather than purely as NO [*Alvarado et al.*, 2010; *Fischer et al.*, 2014]. Anthropogenic emissions for all short-lived species, including NO and NH_3, are from the Community Emissions Data System (v2017-05-18) [*Hoesly et al.*, 2017] developed in support of the Coupled Model Intercomparison Project Phase 6 (CMIP6). This inventory improves the spatial (0.5° × 0.5° versus 1° × 1°) and seasonal (monthly for each year versus annual for each decade) distribution of anthropogenic emissions compared with the inventory used for CMIP5 [*Lamarque et al.*, 2010].

To facilitate comparisons with satellite observations, AM3 is run at a horizontal resolution of 0.5° × 0.5° and model horizontal winds are nudged to 6-hourly horizontal winds from the National Centers for Environmental Prediction reanalysis [*Kalnay et al.*, 1996; *Lin et al.*, 2012]. Monthly sea surface temperature and sea ice cover are prescribed following *Taylor et al.* [2000] and *Rayner et al.* [2003]. For comparison with IASI, we sample the model at the time and location of valid observations of both CO and NH_3. No averaging kernel is produced in the IASI retrieval of NH_3, so we compare simulated columns directly with observations selected based on the relative and absolute error. This approach helps reduce the high bias associated with regridding based solely on relative errors [*Van Damme et al.*, 2014; *Whitburn et al.*, 2016b].

The molar enhancement ratio of X relative to CO in biomass burning plumes is defined as

$$\mathrm{ER}_{X/\mathrm{CO}} = \frac{[X] - [X]_{\mathrm{background}}}{[\mathrm{CO}] - [\mathrm{CO}]_{\mathrm{background}}}$$

$\mathrm{ER}_{\mathrm{NH_3/CO}}$ can be estimated from satellite observations using the slope of the relationship between CO and NH_3 column burdens [*Coheur et al.*, 2009; *Whitburn et al.*, 2016a]. As CO emissions are much better constrained than NH_3, $\mathrm{ER}_{\mathrm{NH_3/CO}}$ can then be used to estimate NH_3 emission factor ($\mathrm{EF}(NH_3)$ in g/kg of dry matter), as $\mathrm{EF}(NH_3) = \mathrm{ER}_{\mathrm{NH_3}} \times \mathrm{EF}(\mathrm{CO}) \times \mathrm{MW}(NH_3)/\mathrm{MW}(\mathrm{CO})$. This approach provides a lower bound for $EF(NH_3)$, as it does not account for the longer lifetime of CO relative to NH_3 [*Whitburn et al.*, 2016a].

3. Results and Discussion

3.1. Enhancement Ratios Over Boreal Forest, Tropical Forest, and Savanna Fires

Figure 1 shows NH_3 emissions from biomass burning in the GFED inventory over the 2009–2013 period. Biomass burning contributes less than 6% of the overall source of NH_3, which is dominated by agriculture [*Bouwman et al.*, 1997; *Paulot et al.*, 2014]. The largest biomass burning sources of NH_3 are located in the southern tropics and in boreal regions. We select three regions—Amazon, South Equatorial Africa, and Alaska—that are representative of tropical forests, savannas, and boreal forests, respectively. Figure 1 shows the observed (black) and simulated (red) time series for NH_3 and CO columns in each region. AM3 captures the magnitude and interannual variability of NH_3 and CO well during the biomass burning season (high NH_3(bb) columns, blue). The overall correlation between simulated and observed columns is greater than 0.57 except for NH_3 in South Equatorial Africa ($R = 0.36$). In this region, *Whitburn et al.* [2015] previously noted that NH_3 and CO columns peak 1 month after the fire radiative power, suggesting an increase in EF in the course of the fire season. The high correlation between simulated and observed CO columns ($R = 0.83$) also suggests that nonfire emissions, which account for 49% of the NH_3 burden annually and 26% during the biomass burning season (July–September), also contribute to the discrepancy between simulated and observed NH_3 columns in this region.

Higher NH_3(bb) column than NH_3 column during the biomass burning season reflects the simulated partitioning of NH_3 to NH_4^+ aerosol. AM3 suggests that significant partitioning occurs in the Amazon in 2010 and South Equatorial Africa, while there is little partitioning in Alaska. During low fire years (2009 and 2011–2013), NH_3(bb) column is lower than the simulated NH_3 column over the Amazon, implying a large influence from nonbiomass burning sources (e.g., agriculture). The simulated NH_4NO_3 column (green) during the biomass burning season is comparable or greater than that of NH_3 in the Amazon in 2010 and South Equatorial Africa. An additional simulation with no NH_3 emissions from biomass burning shows that fires are a major source of NH_4NO_3 in these regions (Figure S1 in the supporting information).

Figure 2 shows the variation in observed and simulated daily $\mathrm{ER}_{\mathrm{NH_3/CO}}$ with varying CO column in the three regions shown in Figure 1 during the biomass burning season (months indicated in plot). Here $\mathrm{ER}_{X/\mathrm{CO}}$ is calculated daily over land in each 2.5° × 2.5° subregions with 10 valid observations and a correlation between CO and NH_3 greater than 0.3 [*Whitburn et al.*, 2016a]. This approach allows us to isolate the effect of fire

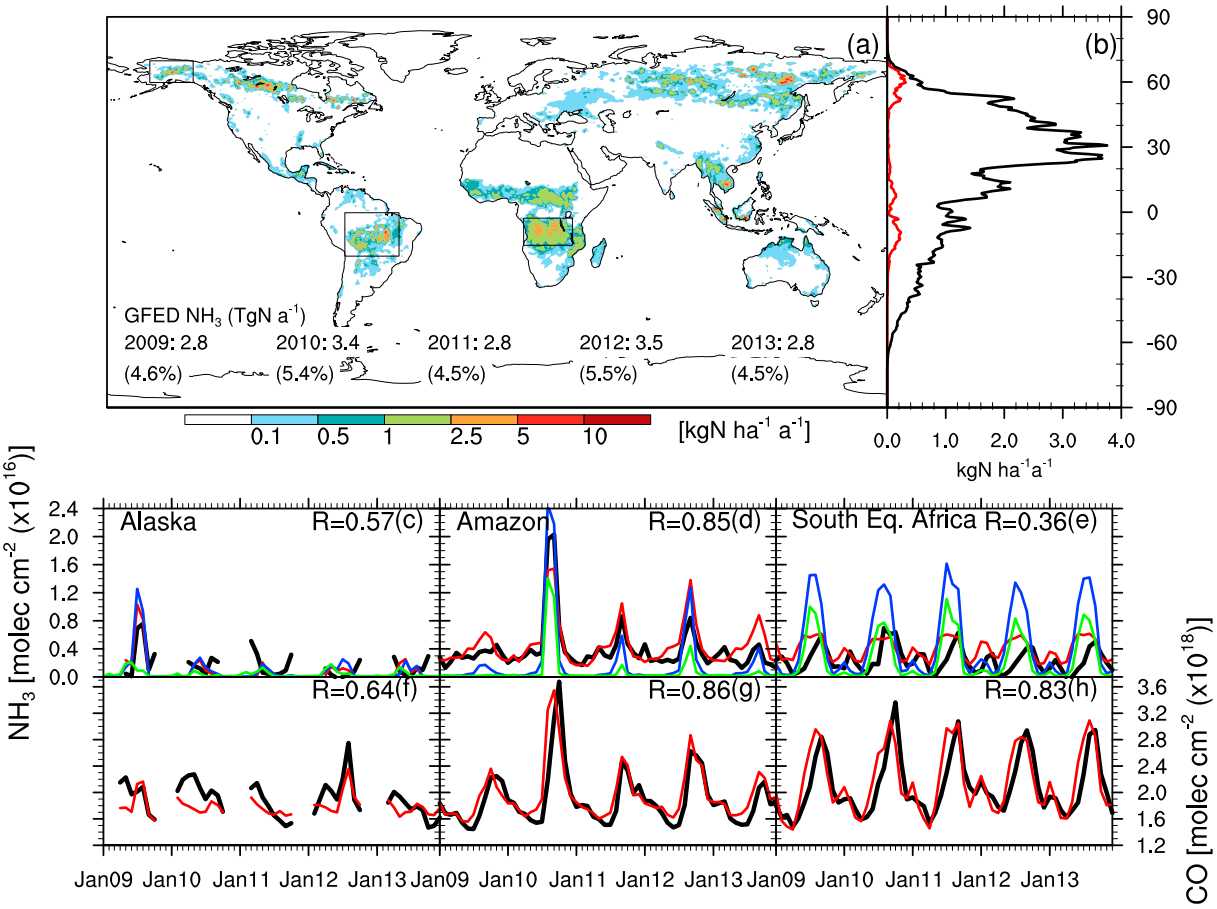

Figure 1. (a) GFED biomass burning emissions of NH_3 and (b) their meridional contribution (red line) to the total emissions of NH_3 (black line) over the 2009–2013 period. The global values of GFED NH_3 emissions and their contribution to the overall NH_3 emissions are shown in insets (Figure 1a). Monthly averaged observed (black) and simulated (red) columns for (c–e) NH_3 and (f–h) CO over land for Western Alaska (Figures 1c and 1f), the Amazon (Figures 1d and 1g), and South Equatorial Africa (Figures 1e and 1h). The simulated columns of NH_4NO_3 and NH_3(bb) (NH_3 emitted from biomass burning with no chemical sink) are also shown in green and blue, respectively. The model is sampled at locations and times when both valid CO and NH_3 observations are available. Months for which more than 50% of the region has no valid observation are not shown. The correlation between observed and simulated columns are indicated in insets.

emissions, which only affect a fraction of each region on any given day, from other emissions. As NH_3 is removed from the atmosphere much faster than CO, one would expect $ER_{NH_3/CO}$ to increase with the CO burden, corresponding to fresher plumes, and approach $EF_{NH_3/CO}$ (dashed line). This ideal behavior is demonstrated by the simulated $ER_{NH_3(bb)/CO}$. However, both observed and simulated $ER_{NH_3/CO}$ decrease with CO column in the Amazon and South Equatorial Africa and the simulated $ER_{NH_3/CO}$ underestimates $EF_{NH_3/CO}$. The decrease in $ER_{NH_3/CO}$ suggests that even during the biomass burning season, NH_3 is significantly affected by nonbiomass burning emissions (most likely agriculture). To limit this influence, we focus on $ER_{NH_3/CO}$ at high CO column amounts, which is taken as a proxy for young fire plumes.

Table 1 shows observed and simulated $ER_{NH_3/CO}$ from biomass burning for the regions shown in Figure 1. Observations of $ER_{NH_3/CO}$ compare well with recent estimates from *Whitburn et al.* [2017]. However, observed and simulated $ER_{NH_3/CO}$ are lower than implied by $EF_{NH_3/CO}$ derived from in situ observations in fresh plumes [*Akagi et al.*, 2011] by 35% in Alaska, 45% in the Amazon, and 70% over South Equatorial Africa. Significant differences have also been reported in previous studies and attributed to (i) misrepresentations of NH_3 emissions, (ii) artifacts in NH_3 retrieval [*Whitburn et al.*, 2017], (iii) differential aging [*Whitburn et al.*, 2015, 2016a]. Errors in NH_3 emissions [*Alvarado et al.*, 2011; *Luo et al.*, 2015; *Whitburn et al.*, 2015, 2016a] are the most common explanation, as EF_{NH_3} remains particularly uncertain with in situ observations showing large natural variability [*Akagi et al.*, 2011]. In addition, changes in the nature of the fire (e.g., degree of flaming) can introduce significant variations in biomass burning emission on diurnal to seasonal time scales, which are not captured

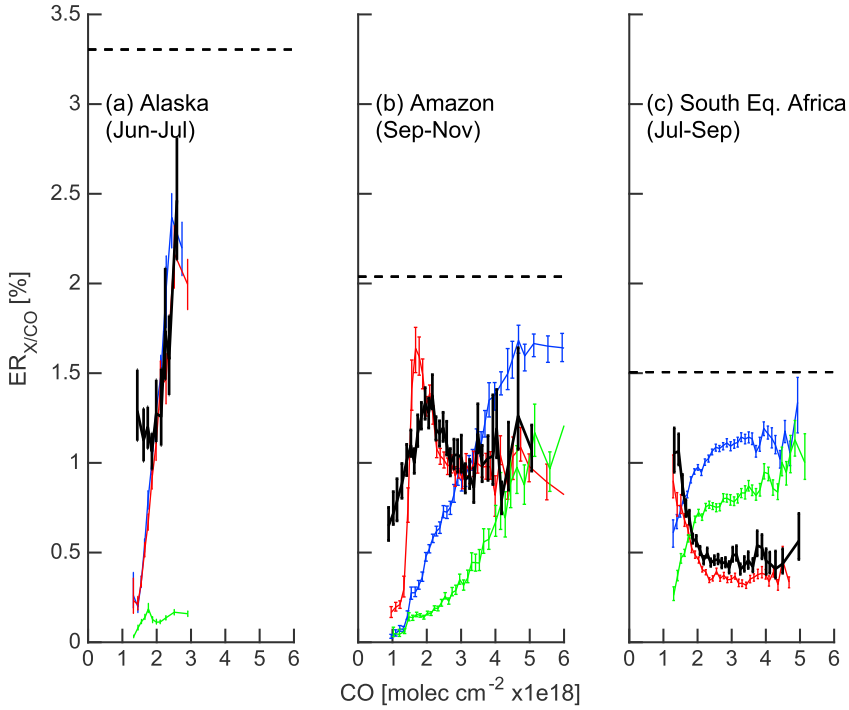

Figure 2. Observed (black) and simulated (red) daily $ER_{NH_3/CO}$ for the three regions shown in Figure 1 during the biomass burning season. Simulated $ER_{NH_4NO_3/CO}$ and $ER_{NH_3(bb)/CO}$ are shown in green and blue, respectively. The dashed black line shows the molar ratio of NH_3 to CO emissions. Each point represents the average of at least 30 daily $ER_{X/CO}$ values. Error bars indicate the bootstrapped 95% confidence interval of the mean.

Table 1. Regional EF and ER Ratios

	Alaska		Amazon		South Equatorial Africa	
	(60°N–70°N, −160°E–140°E)		(−20°N–0°N, −70°E–45°E)		(−15°N–−2.5°N, 12.5°E–35°E)	
Dominant vegetation	Boreal		Tropical Forest		Savanna	
$EF_{NH_3/CO}$(%)[a]	3.3		2.0		1.5	
$ER_{NH_3/CO}$(%)[b]						
IASI[c]	2.1	[1.6–2.7]	1.1	[0.9–1.3]	0.45	[0.4–0.5]
AM3	2.0	[1.8–2.2]	0.97	[0.9–1.1]	0.35	[0.3–0.4]
AM3 (NH_3(bb))	2.3	[2.1–2.5]	1.6	[1.5–1.7]	1.12	[1.1–1.2]
$ER_{NO_3^-/CO}$(%)						
AM3[b]	0.16	[0.1–0.2]	0.96	[0.8–1.1]	0.86	[0.8–0.9]
Aircraft	0.06–0.18[d]				0.32 ± 0.55[e]	
EF_{NO_x/NH_3}(mol/mol)[a]	0.18		1.85		3.6	

[a]Molar emission ratio in GFED (http://www.falw.vu/~gwerf/GFED/GFED4/ancill/). Natural variability in NH_3 emissions for these biomes is >65% [*Akagi et al.*, 2011].

[b]Mean molar enhancement of *X* relative to CO. We only consider CO columns greater than 2.5×10^{18} molecules cm^{-2} (Alaska), 4×10^{18} molecules cm^{-2} (Amazon), and 3×10^{18} molecules cm^{-2} (South Equatorial Africa) to isolate biomass burning plumes. The correlations between NH_3 and CO are $R = 0.73$, 0.63, and 0.57 for the Alaska, Amazon, and South Equatorial Africa regions, respectively. The 95% bootstrapped confidence interval of the mean is indicated in bracket.

[c]The derived $ER_{NH_3/CO}$ is a lower bound [*Dammers et al.*, 2017].

[d]*Alvarado et al.* [2010].

[e]*Formenti et al.* [2003].

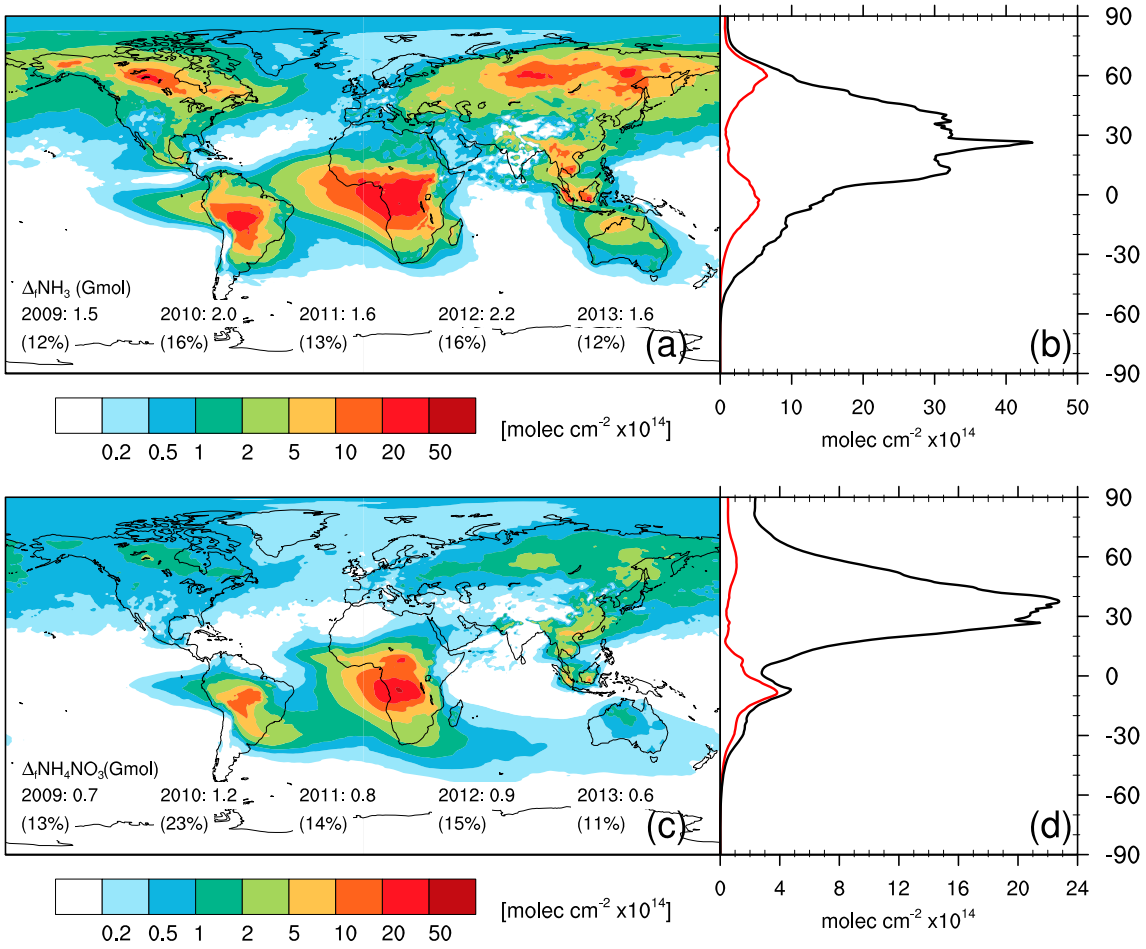

Figure 3. Change in the (a) NH_3 and (c) NH_4NO_3 columns associated with NH_3 emissions from biomass burning. The absolute and relative contribution of biomass burning to the NH_3 ($\Delta_f NH_3$) and NH_4NO_3 ($\Delta_f NH_4NO_3$) global burdens are shown in insets. The contribution of biomass burning (red) to the overall burden (black) of NH_3 and NH_4NO_3 as a function of latitude are shown in Figures 3b and 3d, respectively.

by GFED [*Whitburn et al.*, 2015]. Recent comparisons with ground-based Fourier transform infrared [*Dammers et al.*, 2016, 2017] show that NH_3 retrieval from IASI has a significant low bias (−50%) which decreases to $\simeq -25\%$ for columns exceeding 1.5×10^{16} mol cm^{-2}. Filtering for high NH_3 columns ($>1.5 \times 10^{16}$ mol cm^{-2}) does not significantly affect the derived $ER_{NH_3/CO}$. This suggests that artifacts in the IASI NH_3 retrieval are likely to introduce a low bias in $ER_{NH_3/CO}$ but that regional differences are robust. Table 1 shows that AM3 captures regional differences between the $EF_{NH_3/CO}$ derived from in situ observations and $ER_{NH_3/CO}$ derived from IASI well. Since AM3 is driven by $EF_{NH_3/CO}$ from in situ observations, this suggests that differential aging can also help resolve the discrepancy between in situ and spaceborne constraints on fire emissions of NH_3.

NH_3 aging can be divided into two components: (1) chemical loss (dominated by its gas-to-aerosol partitioning [*Paulot et al.*, 2016]) and (2) deposition loss and mixing. In our simulations, the difference between $ER_{NH_3/CO}$ and $ER_{NH_3(bb)/CO}$ is a measure of the former, while the difference between $ER_{NH_3(bb)/CO}$ and $EF_{NH_3/CO}$ is a measure of the latter. Table 1 shows that the ratio of $ER_{NH_3(bb)/CO}$ to $EF_{NH_3/CO}$ is similar (0.7–0.8) in all regions. In contrast, the ratio of $ER_{NH_3/CO}$ to $ER_{NH_3(bb)/CO}$ ranges from 0.9 in Alaska to 0.3 in South Equatorial Africa. This range implies that regional differences in the degree of partitioning of NH_3 to NH_4^+ can induce larger differences in $ER_{NH_3/CO}$ than differences in $EF_{NH_3/CO}$. In AM3, the degree of partitioning to aerosol is largely driven by the formation of NH_4NO_3 and increases with EF_{NO_x/NH_3}. Observations also show higher $ER_{NH_4NO_3/CO}$ over savanna fires than boreal fires (Table 1). Note that high EF_{NO_x/NH_3} alone is not a sufficient condition for a large fraction of NH_3 to partition to NH_4NO_3. Emissions of NH_3 and NO also need to be sufficiently large for the product of TNH_3 and TNO_3 to exceed the dissociation constant for NH_4NO_3 [*Seinfeld and Pandis*, 2006; *Bellouin et al.*, 2011]. Injection of smoke above the boundary layer also increases the production of NH_4NO_3,

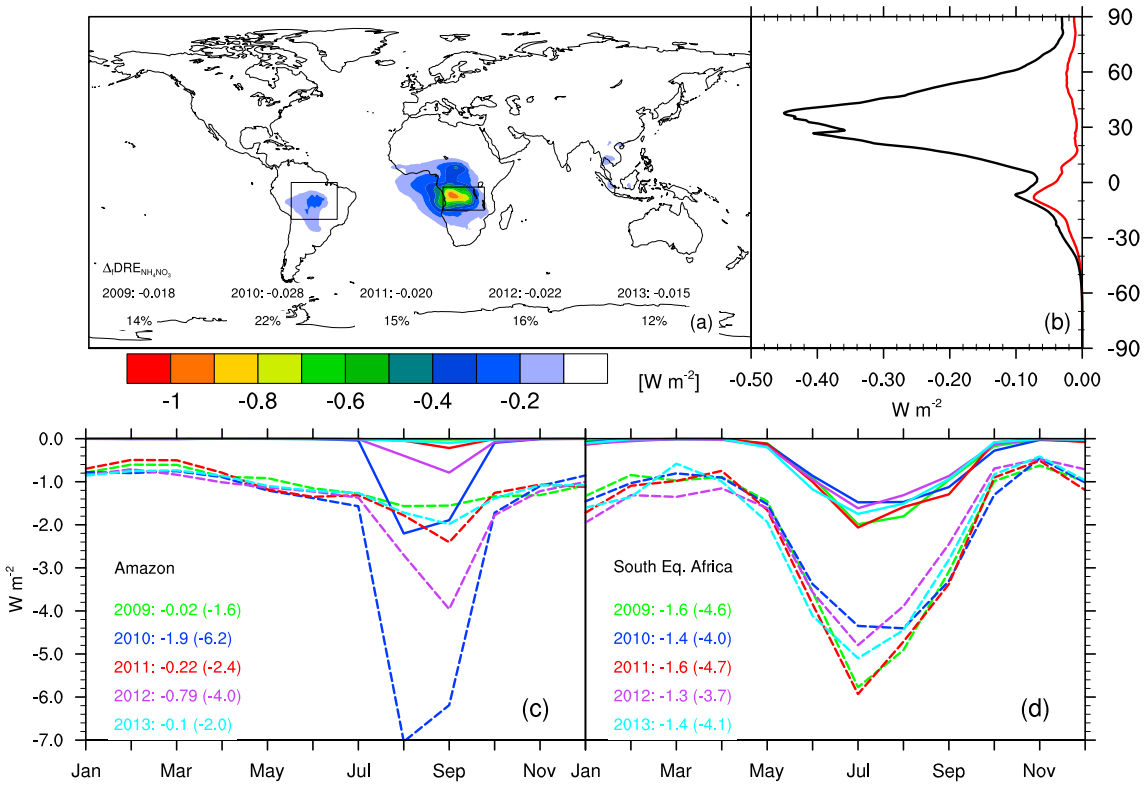

Figure 4. (a) Top-of-atmosphere all-sky direct radiative effect (DRE) associated with NH_4NO_3 from biomass burning ($\Delta_f DRE_{NH_4NO_3(bb)}$), in W m^{-2}. The global values of $\Delta_f DRE_{NH_4NO_3}$ and their contributions to the $DRE_{NH_4NO_3}$ are shown in insets. (b) The zonal mean $DRE_{NH_4NO_3}$ (black) and the contribution from biomass burning (red). $\Delta_f DRE_{NH_4NO_3}$ (solid) and $DRE_{aerosol}$ (dashed) over the (c) Amazon and (d) South Equatorial Africa. The value of $\Delta_f DRE_{NH_4NO_3}$ and $DRE_{aerosol}$ (in parentheses) are indicated in inset for each year for both the Amazon (September) and South Equatorial Africa (July–September).

as its dissociation constant decreases more than 200-fold from 25°C to 5°C (at RH = 50% [*Seinfeld and Pandis*, 2006]). AM3 suggests that these conditions for NH_4NO_3 production are often not met over the Amazon in low fire years, highlighting the nonlinear response of NH_4NO_3 to fire intensity. Simulations with global perturbations of NH_3 emissions from biomass burning further show that the resulting change in the degree of limitation of NH_4NO_3 by NH_3 modulates the relationship between $ER_{NH_3/CO}$ and $EF_{NH_3/CO}$ (Table S1).

3.2. Implication for the Contribution of Biomass Burning to the Burden and Direct Radiative Effect of Ammonium Nitrate

We performed an additional simulation with no emission of NH_3 from biomass burning to estimate the impact on the global burden of NH_3 and NH_4NO_3. Figure 3 shows that fires contribute 12 to 16% (yearly values shown as inset) of the overall NH_3 burden ($\Delta_f NH_3$) from 2009 to 2013, more than the contribution of fires to the overall source of NH_3 ($\simeq$ 5%, Figure 1). This high sensitivity can be partly attributed to the injection of NH_3 into the free troposphere, which reduces its surface removal. This injection in a region where NH_4NO_3 production is limited by NH_3 [*Paulot et al.*, 2016] and the elevated concentration of TNH_3 and TNO_3 in fire plumes also result in a large contribution of NH_3 from fires (up to 23%) to the NH_4NO_3 burden ($\Delta_f NH_4NO_3$). The spatial distribution of $\Delta_f NH_3$ and its interannual variability closely follow the variations of the biomass burning source of NH_3, peaking in the tropics and boreal regions (see also Figure S1). In contrast, tropical and southern subtropical regions (−35°S to 15°N) account for 75% of $\Delta_f NH_4NO_3$ and dominate its interannual variability. The importance of the tropics for $\Delta_f NH_4NO_3$ is illustrated by the contrast between 2010 (high fires in South America) and 2012 (high fire in boreal Asia). Both years have similar global NH_3 emissions from fires (Figure 1), but $\Delta_f NH_4NO_3$ is 50% larger in 2010 than in 2012, consistent with the much higher $EF(NO_x)$ in tropical forest fires than boreal forest fires (Table 1).

We then estimate the contribution of biomass burning to the top of atmosphere (TOA) direct radiative effect of NH_4NO_3 ($DRE_{NH_4NO_3}$), i.e., the instantaneous radiative impact of NH_4NO_3 [*Heald et al.*, 2014]. DRE_X is calculated as the difference between the instantaneous TOA radiative imbalance with and without *X*

[*Ming et al.*, 2005], which are obtained by calling the radiative transfer scheme twice at each time step. The simulated annual global mean $DRE_{NH_4NO_3}$ are −0.13 and −0.21 W m^{-2} for all-sky and clear-sky conditions, respectively, over the 2009–2013 period (Figures S2 and S3). This is in reasonable agreement with previous estimates from *Heald et al.* [2014] (−0.086 and −0.122 W m^{-2}, after we rescale from NO_3^- to NH_4NO_3 using the ratio of $MW(NH_4NO_3^-)$ to $MW(NH_3^-)$) and with the multimodel mean all-sky TOA direct radiative forcing (DRF) (a lower bound for DRE [*Heald et al.*, 2014]) from AEROCOM II [*Myhre et al.*, 2013b]: $DRF_{NH_4NO_3} = -0.08$ (−0.02 to −0.12) W m^{-2} from 1850 to 2000 and $DRF_{NH_4NO_3} = -0.11$ W m^{-2} from 1750 to 2010. The global $DRE_{NH_4NO_3}$ associated with biomass burning ($\Delta_f DRE_{NH_4NO_3}$) is calculated as the difference of $DRE_{NH_4NO_3}$ with and without NH_3 emissions from biomass burning. Over the 2009–2013 period $\Delta_f DRE_{NH_4NO_3}$ is −0.02 W m^{-2} (Figure 4) and −0.03 W m^{-2} (Figure S4) for all-sky and clear-sky conditions, respectively, much less than estimated for black carbon (0.03–0.4 W m^{-2}) and organic carbon (−0.4 to −0.03 W m^{-2}) [*Myhre et al.*, 2013a; *Saleh et al.*, 2015]. $\Delta_f DRE_{NH_4NO_3}$ is most negative in the tropics (< −1 W m^{-2} in South Equatorial Africa). Figure 4 also shows its seasonality and interannual variability over the Amazon and South Equatorial Africa (see also Figures S4 and S5 and *Sena et al.* [2013]). $\Delta_f DRE_{NH_4NO_3}$ reaches −1.9 W m^{-2} and −1.6 W m^{-2} during the biomass burning season over the Amazon and South Equatorial Africa, respectively, highlighting the regional importance of NH_4NO_3 produced from biomass burning.

4. Conclusion

We have derived $ER_{NH_3/CO}$ using column burdens from IASI over tropical forest, savanna, and boreal forest fires. $ER_{NH_3/CO}$ is lower than $EF_{NH_3/CO}$ derived from in situ observations by 30% over boreal forest, 45% over tropical forest, and 70% over savanna fires. Similar discrepancies have been reported in previous studies and interpreted in terms of misrepresentations in NH_3 emissions. However, we show that the AM3 global chemistry-climate model captures the observed $ER_{NH_3/CO}$ well when driven by $EF_{NH_3/CO}$ derived from in situ observations. We estimate that dilution and deposition can result in a 30% decrease of $ER_{NH_3/CO}$ (as observed by IASI) relative to $EF_{NH_3/CO}$. The larger discrepancy over tropical forest and savanna fires is attributed to the rapid partitioning of NH_3 to NH_4^+. Our model predicts that the relative impact of this partitioning is greatest in savanna fires, as high EF_{NO_x/NH_3} allows for the efficient production of NH_4NO_3. The large simulated spatial and interannual variability in the impact of aging on $ER_{NH_3/CO}$ suggest that models that resolve the chemistry of NH_3 and NH_4NO_3 are needed to interpret spaceborne observations of NH_3 and that in situ constraints on its fate in fire plumes are urgently needed. Our conclusions are likely to be applicable to other sources of NH_3. For instance, *Warner et al.* [2017] recently noted that the observed increase in the NH_3 column over Europe may be driven by the decrease in the emissions of SO_4^{2-} and HNO_3 precursors rather than by changes in NH_3 emissions.

Biomass burning is estimated to contribute 11–23% of the NH_4NO_3 burden and 12%–22% of $DRE_{NH_4NO_3}$ (−15––28 mW m^{-2}). This exceeds the contribution of fires to the overall NH_3 emissions (≃ 5% in our simulation). This high sensitivity is driven by the collocation of high concentrations of TNH_3 and TNO_3 in fire plumes and by the injection of NH_3 in the free troposphere, where NH_4NO_3 production is more frequently limited by NH_3 than at the surface. NH_4NO_3 production is largest in South Equatorial regions (colocated with high EF_{NO_x/NH_3}), where biomass burning is simulated to be its single largest source, with $\Delta_f DRE_{NH_4NO_3}$ as low as −1.9 W m^{-2} during the biomass burning season over the Amazon. Our model shows that significant production of NH_4NO_3 only occurs in large fires, contributing to significant interannual variability of $\Delta_f DRE_{NH_4NO_3}$. This suggests that the increase in fire activity associated with deforestation in the Amazon [*van Marle et al.*, 2017] has made NH_4NO_3 production more likely in this region. The simulated regional and interannual variability in the production of NH_4NO_3 may also have important implications for the overall radiative properties of smoke both directly and indirectly, as mixing of NH_4NO_3 with organic carbon has been shown to increase the absorption of organic carbon ("lensing" effect [*Lack et al.*, 2012; *Saleh et al.*, 2015]).

Acknowledgments
This study was supported by NOAA Climate Program Office's Atmospheric Chemistry, Carbon Cycle, and Climate program and by NASA grant NNH14ZDA001N-ACMAP to P. Ginoux. S. Whitburn is grateful for his PhD grant (Boursier FRIA) to the "Fonds pour la Formation à la Recherche dans l'Industrie et dans l'Agriculture" of Belgium. L. Clarisse is a research associate with the Belgian F.R.S-FNRS. We thank S. Fan, J. Schnell, and two anonymous reviewers for helpful comments. The output of AM3 simulations is available upon request (Fabien.Paulot@noaa.gov). IASI observations can be obtained at http://www.pole-ether.fr.

References

Akagi, S. K., R. J. Yokelson, C. Wiedinmyer, M. J. Alvarado, J. S. Reid, T. Karl, J. D. Crounse, and P. O. Wennberg (2011), Emission factors for open and domestic biomass burning for use in atmospheric models, *Atmos. Chem. Phys.*, *11*, 4039–4072.

Akagi, S. K., et al. (2012), Evolution of trace gases and particles emitted by a chaparral fire in California, *Atmos. Chem. Phys.*, *12*, 1397–1421.

Alvarado, M. J., K. E. Cady-Pereira, Y. Xiao, D. B. Millet, and V. H. Payne (2011), Emission ratios for ammonia and formic acid and observations of Peroxy Acetyl Nitrate (PAN) and ethylene in biomass burning smoke as seen by the Tropospheric Emission Spectrometer (TES), *Atmosphere*, *2*, 633–654.

Alvarado, M. J., et al. (2010), Nitrogen oxides and PAN in plumes from boreal fires during ARCTAS-B and their impact on ozone: An integrated analysis of aircraft and satellite observations, *Atmos. Chem. Phys.*, *10*, 9739–9760.
Andreae, M. O., and P. Merlet (2001), Emission of trace gases and aerosols from biomass burning, *Global Biogeochem. Cycles*, *15*, 955–966.
Bellouin, N., J. Rae, A. Jones, C. Johnson, J. Haywood, and O. Boucher (2011), Aerosol forcing in the Climate Model Intercomparison Project (CMIP5) simulations by HadGEM2-ES and the role of ammonium nitrate, *J. Geophys. Res.*, *116*, D20206, doi:10.1029/2011JD016074.
Benedict, K. B., A. J. Prenni, C. M. Carrico, A. P. Sullivan, B. A. Schichtel, and J. L. Jr. Collett (2017), Enhanced concentrations of reactive nitrogen species in wildfire smoke, *Atmos. Environ.*, *148*, 8–15.
Bouwman, A. F., D. S. Lee, W. A. H. Asman, F. J. Dentener, K. W. Van Der Hoek, and J. G. J. Olivier (1997), A global high-resolution emission inventory for ammonia, *Global Biogeochem. Cycles*, *11*, 561–587.
Cai, C., et al. (2016), Simulating reactive nitrogen, carbon monoxide, and ozone in California during ARCTAS-CARB 2008 with high wildfire activity, *Atmos. Environ.*, *128*, 28–44.
Chen, Y., J. T. Randerson, G. R. van der Werf, D. C. Morton, M. Mu, and P. S. Kasibhatla (2010), Nitrogen deposition in tropical forests from savanna and deforestation fires, *Global Change Biol.*, *16*, 2024–2038.
Coheur, P.-F., L. Clarisse, S. Turquety, D. Hurtmans, and C. Clerbaux (2009), IASI measurements of reactive trace species in biomass burning plumes, *Atmos. Chem. Phys.*, *9*, 5655–5667.
Collier, S., et al. (2016), Regional influence of aerosol emissions from wildfires driven by combustion efficiency: Insights from the BBOP campaign, *Environ. Sci. Technol.*, *50*, 8613–8622.
Dammers, E., et al. (2016), An evaluation of IASI-NH3 with ground-based Fourier transform infrared spectroscopy measurements, *Atmos. Chem. Phys.*, *16*, 10,351–10,368.
Dammers, E., et al. (2017), Validation of the CrIS fast physical NH3 retrieval with ground-based FTIR, *Atmos. Meas. Tech. Discuss.*, *10*, 2645–2667.
Donner, L. J., et al. (2011), The dynamical core, physical parameterizations, and basic simulation characteristics of the atmospheric component AM3 of the GFDL global coupled model CM3, *J. Clim.*, *24*, 3484–3519.
Fischer, E. V., et al. (2014), Atmospheric peroxyacetyl nitrate (PAN): A global budget and source attribution, *Atmos. Chem. Phys.*, *14*, 2679–2698.
Formenti, P., W. Elbert, W. Maenhaut, J. Haywood, S. Osborne, and M. O. Andreae (2003), Inorganic and carbonaceous aerosols during the Southern African Regional Science Initiative (SAFARI 2000) experiment: Chemical characteristics, physical properties, and emission data for smoke from African biomass burning, *J. Geophys. Res.*, *108*(D13), 8488, doi:10.1029/2002JD002408.
Fountoukis, C., and A. Nenes (2007), ISORROPIA II: A computationally efficient thermodynamic equilibrium model for $K^+ - Ca^{2+} - Mg^{2+} - NH_4^+ - Na^+ - SO_4^{2-} - NO_3^- - Cl^- - H_2O$ aerosols, *Atmos. Chem. Phys.*, *7*, 4639–4659.
Giglio, L., J. T. Randerson, G. R. van der Werf, P. S. Kasibhatla, G. J. Collatz, D. C. Morton, and R. S. DeFries (2010), Assessing variability and long-term trends in burned area by merging multiple satellite fire products, *Biogeosciences*, *7*, 1171–1186.
Gosse, S. F., M. Wang, D. Labrie, and P. Chylek (1997), Imaginary part of the refractive index of sulfates and nitrates in the 07–26-μm spectral region, *Appl. Opt.*, *36*, 3622–3634.
Griffies, S. M., et al. (2011), The GFDL CM3 coupled climate model: Characteristics of the ocean and sea ice simulations, *J. Clim.*, *24*, 3520–3544.
Hauglustaine, D. A., Y. Balkanski, and M. Schulz (2014), A global model simulation of present and future nitrate aerosols and their direct radiative forcing of climate, *Atmos. Chem. Phys.*, *14*, 11,031–11,063.
Heald, C. L., et al. (2012), Atmospheric ammonia and particulate inorganic nitrogen over the United States, *Atmos. Chem. Phys.*, *12*, 10,295–10,312.
Heald, C. L., D. A. Ridley, J. H. Kroll, S. R. H. Barrett, K. E. Cady-Pereira, M. J. Alvarado, and C. D. Holmes (2014), Contrasting the direct radiative effect and direct radiative forcing of aerosols, *Atmos. Chem. Phys.*, *14*, 5513–5527.
Hecobian, A., et al. (2011), Comparison of chemical characteristics of 495 biomass burning plumes intercepted by the NASA DC-8 aircraft during the ARCTAS/CARB-2008 field campaign, *Atmos. Chem. Phys.*, *11*, 13,325–13,337.
Hobbs, P. V., P. Sinha, R. J. Yokelson, T. J. Christian, D. R. Blake, S. Gao, T. W. Kirchstetter, T. Novakov, and P. Pilewskie (2003), Evolution of gases and particles from a savanna fire in South Africa, *J. Geophys. Res.*, *108*(D13), 8485, doi:10.1029/2002JD002352.
Hoesly, R. M., et al. (2017), Historical (1750–2014) anthropogenic emissions of reactive gases and aerosols from the Community Emission Data System (CEDS), *Geosci. Model Dev. Discuss.*, *2017*, 1–41.
Hurtmans, D., P. F. Coheur, C. Wespes, L. Clarisse, O. Scharf, C. Clerbaux, J. Hadji-Lazaro, M. George, and S. Turquety (2012), FORLI radiative transfer and retrieval code for IASI, *J. Quant. Spectrosc. Radiat. Transfer*, *113*, 1391–1408.
John, J. G., A. M. Fiore, V. Naik, L. W. Horowitz, and J. P. Dunne (2012), Climate versus emission drivers of methane lifetime against loss by tropospheric OH from 1860–2100, *Atmos. Chem. Phys.*, *12*, 12,021–12,036.
Kaiser, J. W., et al. (2012), Biomass burning emissions estimated with a global fire assimilation system based on observed fire radiative power, *Biogeosciences*, *9*, 527–554.
Kalnay, E., et al. (1996), The NCEP/NCAR 40-year reanalysis project, *Bull. Am. Meteorol. Soc.*, *77*, 437–471.
Lack, D. A., J. M. Langridge, R. Bahreini, C. D. Cappa, A. M. Middlebrook, and J. P. Schwarz (2012), Brown carbon and internal mixing in biomass burning particles, *Proc. Natl. Acad. Sci. U.S.A.*, *109*, 14,802–14,807.
Lamarque, J.-F., et al. (2010), Historical (1850–2000) gridded anthropogenic and biomass burning emissions of reactive gases and aerosols: Methodology and application, *Atmos. Chem. Phys.*, *10*, 7017–7039.
Lin, M., et al. (2012), Transport of Asian ozone pollution into surface air over the western United States in spring, *J. Geophys. Res.*, *117*, D00V07, doi:10.1029/2011JD016961.
Liu, X., et al. (2016), Agricultural fires in the southeastern U.S. during SEAC4rs: Emissions of trace gases and particles and evolution of ozone, reactive nitrogen, and organic aerosol, *J. Geophys. Res. Atmos.*, *121*, 7383–7414, doi:10.1002/2016JD025040.
Luo, M., et al. (2015), Satellite observations of tropospheric ammonia and carbon monoxide: Global distributions, regional correlations and comparisons to model simulations, *Atmos. Environ.*, *106*, 262–277.
Lutsch, E., E. Dammers, S. Conway, and K. Strong (2016), Long-range transport of NH_3, CO, HCN, and C_2h_6 from the 2014 Canadian Wildfires, *Geophys. Res. Lett.*, *43*, 8286–8297, doi:10.1002/2016GL070114.
Ming, Y., V. Ramaswamy, P. A. Ginoux, and L. H. Horowitz (2005), Direct radiative forcing of anthropogenic organic aerosol, *J. Geophys. Res.*, *110*, D20208, doi:10.1029/2004JD005573.
Mu, M., et al. (2011), Daily and 3-hourly variability in global fire emissions and consequences for atmospheric model predictions of carbon monoxide, *J. Geophys. Res.*, *116*, D24303, doi:10.1029/2011JD016245.
Myhre, G., et al. (2013a), *Anthropogenic and Natural Radiative Forcing*, book section 8, pp. 659–740, Cambridge Univ. Press, Cambridge, U. K., and New York.

Myhre, G., et al. (2013b), Radiative forcing of the direct aerosol effect from AeroCom phase II simulations, *Atmos. Chem. Phys.*, *13*, 1853–1877.
Naik, V., L. W. Horowitz, A. M. Fiore, P. Ginoux, J. Mao, A. M. Aghedo, and H. Levy (2013), Impact of preindustrial to present-day changes in short-lived pollutant emissions on atmospheric composition and climate forcing, *J. Geophys. Res. Atmos.*, *118*, 8086–8110, doi:10.1002/jgrd.50608.
Paton-Walsh, C., N. B. Jones, S. R. Wilson, V. Haverd, A. Meier, D. W. T. Griffith, and C. P. Rinsland (2005), Measurements of trace gas emissions from Australian forest fires and correlations with coincident measurements of aerosol optical depth, *J. Geophys. Res.*, *110*, D24305, doi:10.1029/2005JD006202.
Paulot, F., and D. J. Jacob (2014), Hidden cost of U.S. agricultural exports: Particulate matter from ammonia emissions, *Environ. Sci. Technol.*, *48*, 903–908.
Paulot, F., D. J. Jacob, R. W. Pinder, J. O. Bash, K. Travis, and D. K. Henze (2014), Ammonia emissions in the United States, European Union, and China derived by high-resolution inversion of ammonium wet deposition data: Interpretation with a new agricultural emissions inventory (MASAGE_NH3), *J. Geophys. Res. Atmos.*, *119*, 4343–4364, doi:10.1002/2013JD021130.
Paulot, F., P. Ginoux, W. F. Cooke, L. J. Donner, S. Fan, M.-Y. Lin, J. Mao, V. Naik, and L. W. Horowitz (2016), Sensitivity of nitrate aerosols to ammonia emissions and to nitrate chemistry: Implications for present and future nitrate optical depth, *Atmos. Chem. Phys.*, *16*, 1459–1477.
Paulot, F., S. Fan, and L. W. Horowitz (2017), Contrasting seasonal responses of sulfate aerosols to declining SO_2 emissions in the eastern U.S.: Implications for the efficacy of SO_2 emission controls, *Geophys. Res. Lett.*, *44*, 455–464, doi:10.1002/2016GL070695.
Pinder, R. W., P. J. Adams, and S. N. Pandis (2007), Ammonia emission controls as a cost-effective strategy for reducing atmospheric particulate matter in the Eastern United States, *Environ. Sci. Technol.*, *41*, 380–386.
Randerson, J. T., Y. Chen, G. R. van der Werf, B. M. Rogers, and D. C. Morton (2012), Global burned area and biomass burning emissions from small fires, *J. Geophys. Res.*, *117*, G04012, doi:10.1029/2012JG002128.
Rayner, N. A., D. E. Parker, E. B. Horton, C. K. Folland, L. V. Alexander, D. P. Rowell, E. C. Kent, and A. Kaplan (2003), Global analyses of sea surface temperature, sea ice, and night marine air temperature since the late nineteenth century, *J. Geophys. Res.*, *108*(D14), 4407, doi:10.1029/2002JD002670.
R'Honi, Y., L. Clarisse, C. Clerbaux, D. Hurtmans, V. Duflot, S. Turquety, Y. Ngadi, and P.-F. Coheur (2013), Exceptional emissions of NH_3 and HCOOH in the 2010 Russian wildfires, *Atmos. Chem. Phys.*, *13*, 4171–4181.
Saleh, R., M. Marks, J. Heo, P. J. Adams, N. M. Donahue, and A. L. Robinson (2015), Contribution of brown carbon and lensing to the direct radiative effect of carbonaceous aerosols from biomass and biofuel burning emissions, *J. Geophys. Res. Atmos.*, *120*, 10,285–10,296, doi:10.1002/2015JD023697.
Schaap, M., M. van Loon, H. M. ten Brink, F. J. Dentener, and P. J. H. Builtjes (2004), Secondary inorganic aerosol simulations for Europe with special attention to nitrate, *Atmos. Chem. Phys.*, *4*, 857–874.
Seinfeld, J. H., and S. N. Pandis (2006), *Atmospheric Chemistry and Physics: From Air Pollution to Climate Change*, John Wiley, New York.
Sena, E. T., P. Artaxo, and A. L. Correia (2013), Spatial variability of the direct radiative forcing of biomass burning aerosols and the effects of land use change in Amazonia, *Atmos. Chem. Phys.*, *13*, 1261–1275.
Sofiev, M., T. Ermakova, and R. Vankevich (2012), Evaluation of the smoke-injection height from wild-land fires using remote-sensing data, *Atmos. Chem. Phys.*, *12*, 1995–2006.
Sofiev, M., R. Vankevich, T. Ermakova, and J. Hakkarainen (2013), Global mapping of maximum emission heights and resulting vertical profiles of wildfire emissions, *Atmos. Chem. Phys.*, *13*, 7039–7052.
Stelson, A. W., and J. H. Seinfeld (1982), Relative humidity and temperature dependence of the ammonium nitrate dissociation constant, *Atmos. Environ.*, *16*, 983–992.
Tang, I. N. (1996), Chemical and size effects of hygroscopic aerosols on light scattering coefficients, *J. Geophys. Res.*, *101*, 19,245–19,250.
Taylor, K. E., D. Williamson, and F. Zwiers (2000), *The Sea Surface Temperature and Sea-Ice Concentration Boundary Conditions for AMIP II Simulations, Program for Climate Model Diagnosis and Intercomparison*, Lawrence Livermore Natl. Lab., Univ. of Calif.
Van Damme, M., L. Clarisse, C. L. Heald, D. Hurtmans, Y. Ngadi, C. Clerbaux, A. J. Dolman, J. W. Erisman, and P. F. Coheur (2014), Global distributions, time series and error characterization of atmospheric ammonia (NH_3) from IASI satellite observations, *Atmos. Chem. Phys.*, *14*, 2905–2922.
van der Werf, G. R., et al. (2010), Global fire emissions and the contribution of deforestation, savanna, forest, agricultural, and peat fires (1997–2009), *Atmos. Chem. Phys.*, *10*, 11,707–11,735.
van Marle, M. J. E., et al. (2017), Historic global biomass burning emissions based on merging satellite observations with proxies and fire models (1750–2015), *Geosci. Model Dev. Discuss.*, *2017*, 1–56.
Warner, J. X., R. R. Dickerson, Z. Wei, L. L. Strow, Y. Wang, and Q. Liang (2017), Increased atmospheric ammonia over the world's major agricultural areas detected from space, *Geophys. Res. Lett.*, *44*, 2875–2884, doi:10.1002/2016GL072305.
Whitburn, S., M. Van Damme, J. W. Kaiser, G. R. van der Werf, S. Turquety, D. Hurtmans, L. Clarisse, C. Clerbaux, and P. F. Coheur (2015), Ammonia emissions in tropical biomass burning regions: Comparison between satellite-derived emissions and bottom-up fire inventories, *Atmos. Environ.*, *121*, 42–54.
Whitburn, S., M. Van Damme, L. Clarisse, S. Turquety, C. Clerbaux, and P.-F. Coheur (2016a), Doubling of annual ammonia emissions from the peat fires in Indonesia during the 2015 El Niño, *Geophys. Res. Lett.*, *43*, 11,007–11,014, doi:10.1002/2016GL070620.
Whitburn, S., M. Van Damme, L. Clarisse, S. Bauduin, C. L. Heald, J. Hadji-Lazaro, D. Hurtmans, M. A. Zondlo, C. Clerbaux, and P.-F. Coheur (2016b), A flexible and robust neural network IASI-NH3 retrieval algorithm, *J. Geophys. Res. Atmos.*, *121*, 6581–6599, doi:10.1002/2016JD024828.
Whitburn, S., M. Van Damme, L. Clarisse, D. Hurtmans, C. Clerbaux, and P.-F. Coheur (2017), IASI-derived NH_3 enhancement ratios relative to CO for the tropical biomass burning regions, *Atmos. Chem. Phys. Discuss.*, *2017*, 1–23.
Yokelson, R. J., et al. (2009), Emissions from biomass burning in the Yucatan, *Atmos. Chem. Phys.*, *9*, 5785–5812.
Yokelson, R. J., M. O. Andreae, and S. K. Akagi (2013), Pitfalls with the use of enhancement ratios or normalized excess mixing ratios measured in plumes to characterize pollution sources and aging, *Atmos. Meas. Tech.*, *6*, 2155–2158.